

A spectral function tour of electron-phonon coupling outside the Migdal limit

C. N. Veenstra,¹ G. L. Goodvin,¹ M. Berciu,^{1,2} and A. Damascelli^{1,2,*}

¹*Department of Physics & Astronomy, University of British Columbia, Vancouver, British Columbia V6T 1Z1, Canada*

²*Quantum Matter Institute, University of British Columbia, Vancouver, British Columbia V6T 1Z4, Canada*

(Dated: August 20, 2018)

We simulate spectral functions for electron-phonon coupling in a filled band system - far from the asymptotic limit often assumed where the phonon energy is very small compared to the Fermi energy in a parabolic band and the Migdal theorem predicting $(1+\lambda)$ quasiparticle renormalizations is valid. These spectral functions are examined over a wide range of parameter space through techniques often used in angle-resolved photoemission spectroscopy (ARPES). Analyzing over 1200 simulations we consider variations of the microscopic coupling strength, phonon energy and dimensionality for two models: a momentum-independent Holstein model, and momentum-dependent coupling to a breathing mode phonon. In this limit we find that any ‘effective coupling’, λ_{eff} , inferred from the quasiparticle renormalizations differs from the microscopic dimensionless coupling characterizing these Hamiltonians, λ , and could drastically either over- or under-estimate it depending on the particular parameters and model. In contrast, we show that perturbation theory retains good predictive power for low coupling and small momenta, and that the momentum-dependence of the self-energy can be revealed via the relationship between velocity renormalization and quasiparticle strength. Additionally we find that (although not strictly valid) it is often possible to infer the self-energy and bare electronic structure through a self-consistent Kramers-Kronig bare-band fitting; and also that through lineshape alone, when Lorentzian, it is possible to reliably extract the shape of the imaginary part of a momentum-dependent self-energy without reference to the bare-band.

PACS numbers: 71.38.-k, 79.60.-i, 74.25.Jb

INTRODUCTION

The many-body problem allows relatively simple interactions to transform into a wide range of exciting yet often complicated phenomena. The quasiparticle picture simplifies these complications by grouping fundamental particles and excitations together into quasiparticles, which themselves behave in a more understandable manner. In this picture the real part of the self-energy represents the energy difference from the bare particle energy, and the imaginary part the inverse lifetime of the combined excitation. Angle-resolved photoemission spectroscopy (ARPES) is a well established tool for the investigation of such electronic systems as it provides access to the electron-removal part of the momentum-resolved spectral function $A(\mathbf{k}, \omega)$ [1], which is generally written in the form:

$$A(\mathbf{k}, \omega) = -\frac{1}{\pi} \frac{\Sigma''(\mathbf{k}, \omega)}{[\omega - \varepsilon_{\mathbf{k}}^b - \Sigma'(\mathbf{k}, \omega)]^2 + [\Sigma''(\mathbf{k}, \omega)]^2}. \quad (1)$$

The analysis of this extremely rich data source can be both difficult and rewarding as it depends on both the interaction self-energy $\Sigma(\mathbf{k}, \omega) = \Sigma'(\mathbf{k}, \omega) + i\Sigma''(\mathbf{k}, \omega)$, as well as the single-particle electronic dispersion $\varepsilon_{\mathbf{k}}^b$ (the so-called ‘bare-band’). A variety of approaches to analyzing this spectral function have been utilized, and often focus on analysis of either quasiparticle dispersions and their path through (\mathbf{k}, ω) space, or lineshape and its implications for the structure of the self-energy. Both methods generally cut the spectral function into curves constant in either momentum (generating a series of energy distribution curves [EDCs]) or energy (for a series of momen-

tum distribution curves [MDCs]). In this work, using simulations which have no experimental limitations, we will perform quasiparticle analysis on EDCs (which allows the identification of a quasiparticle peak in each \mathbf{k} slice thereby forming a quasiparticle dispersion, $\varepsilon_{\mathbf{k}}^q$) and self-energy analysis on MDCs (as self-energies often show stronger energy dependence, allowing the approximation of a constant value over a slice of constant energy).

In quasiparticle analysis one can estimate properties such as the dispersion’s velocity $v_{\mathbf{k}}^q = \partial\varepsilon_{\mathbf{k}}^q/\partial\mathbf{k}$, effective mass $m_{\mathbf{k}}^q$, where $1/m_{\mathbf{k}}^q = \partial^2\varepsilon_{\mathbf{k}}^q/\partial\mathbf{k}^2$, and quasiparticle strength $Z_{\mathbf{k}}^q$, where $Z_{\mathbf{k}}^q = \int^q A(\mathbf{k}, \omega)d\omega$ is the integral over the coherent part of the spectral function (this is the quasiparticle weight only, which in a somewhat loose terminology is often referred to as *quasiparticle coherence* [1]). If the bare-band dispersion $\varepsilon_{\mathbf{k}}^b$ is known, the renormalization of these properties can also be calculated. This concept has been used to generate an ‘effective coupling’ (which we will denote λ_{eff} , but which is often denoted simply λ in ARPES literature) in the analysis of many complex systems, often through the so-called ‘mass enhancement factor’ $m_{\mathbf{k}}^b/m_{\mathbf{k}}^q = v_{\mathbf{k}}^q/v_{\mathbf{k}}^b = Z_{\mathbf{k}}^q = 1/(1+\lambda_{\text{eff}})$. This factor has become a de facto standard in ARPES analysis [1–5] since, in the Migdal/Eliashberg limit after few approximations, it is equivalent to the true dimensionless microscopic coupling found in the Hamiltonian (denoted λ here and in theoretical literature) and is expected to manifest itself in a variety of different measurements [6, 7]. However, the large values sometimes measured for these renormalizations and effective couplings via ARPES (see, for example, Refs. 8–11), should raise the question of this scheme’s universal utility [12–

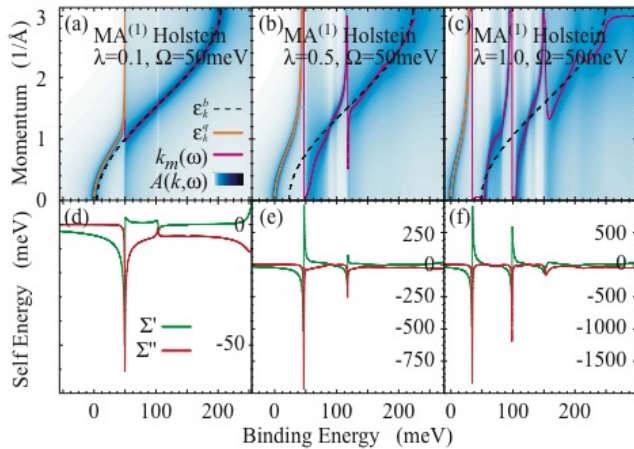


FIG. 1: (Color online). The spectral function (a-c) and self-energies (d-f) for the 1D momentum-independent Holstein polaron model calculated with MA⁽¹⁾ for $\Omega = 50$ meV and different microscopic couplings, with the bare-band ε_k^b , quasi-particle band ε_k^q , and $k_m(\omega)$ path shown.

16], and generally whether the limits implied by such analysis do apply to all systems being measured [17–20].

Another common goal of spectral function analysis is to extract the self-energy. In most circumstances, under the assumption of \mathbf{k} -independence of the self-energy, MDCs cuts through Eq. 1 reduce to a simple Lorentzian form, thus allowing a measurement of $\Sigma'(\omega)$ and $\Sigma''(\omega)$ through ARPES [3, 12, 21–25]. However not only do these methods hinge on some assumptions and/or approximations for the bare-band ε_k^b , but more fundamentally the problem of how momentum-dependence in $\Sigma'(\mathbf{k}, \omega)$ and $\Sigma''(\mathbf{k}, \omega)$ affects this analysis is unaddressed - even though it is known that a Lorentzian line shape does not guarantee a momentum-independent self-energy [26].

Here we present a methodological study of established methods and present some new variations using one of the most studied interactions - that of electrons and phonons. We generate self-energies and spectral functions where the inclusion of momentum-dependence and all energy scales are controlled using the least complicated electron-phonon interaction models possible. However, these models lie outside the limits of Migdal’s theorem [27] where the Eliashberg textbook definition of $(1 + \lambda)$ renormalization is expected to be valid. Before we delve into our findings for quasiparticle and self-energy analysis, we will first illustrate some aspects of our chosen models and how they are simulated.

THE MODELS

We use single electron addition to an empty band to simulate photoemission from a completely filled sys-

tem, at 0 Kelvin. Note that this case can be exactly mapped onto that of a single particle added to an empty band through particle-hole symmetry, which essentially amounts to replacing $\omega \rightarrow -\omega$. This is an ideal test case as it provides the simplest possible description of electron-phonon coupling and is uncomplicated by further interactions such as strong correlations between electrons (as in, for example, Ref. 28), or even a Fermi sea which would add yet another energy scale to the problem (as in, for example, Refs. 29, 30). The chemical potential in our treatment is then the top of the first electron removal state, labelled as 0 binding energy on all plots. For momentum-independent study we will use spectral functions and self-energies generated with the momentum-average approximation MA⁽¹⁾ [31, 32]. Since MA⁽¹⁾ has been shown to be accurate everywhere in parameter space [32], it will enable us to study $A(\mathbf{k}, \omega)$ and $\Sigma(\omega)$ over a broad range of electron-phonon coupling and phonon energies. For momentum-dependent study we use an extension of this approximation with variational considerations, denoted MA^(v,n) [33]. Although generally accurate everywhere in parameter space, for reasons specific to this approximation details studied through EDC quasiparticle analysis are best realized through MA^(v,1), and MDC based self-energy analysis is best realized through MA^(v,0) [48]. In all cases the spectral function remains entirely self-consistent with the associated self-energy.

Our test case for a momentum-independent self-energy is the simplest possible in momentum space, namely the Holstein polaron [34]: momentum-independent coupling between a single dispersionless phonon mode and tight-binding electrons. In reality however, even for the Holstein model, the self-energy is weakly dependent on momentum, which can be seen at the MA⁽²⁾ level of approximation [32]. We overcome this by choosing the momentum-independent self-energy from the MA⁽¹⁾ level in order to see how well these methods work for a truly momentum-independent self energy. For strongly momentum-dependent self-energy study we will model coupling to a single optical mode where the phonons live on half-integer lattice sites in between the electron sites and modify the on-site energy of their neighbours. In 2D this describes lattice vibrations in a CuO₂-like plane, where the motion of the O ions is the most important vibrational degree of freedom; this has been the topic of many ARPES studies [10, 21–23]. Throughout the paper we will refer to this as the breathing-mode model.

We may write both these models in the following form in momentum-space:

$$\mathcal{H} = \sum_{\mathbf{k}} \varepsilon_{\mathbf{k}}^b c_{\mathbf{k}}^{\dagger} c_{\mathbf{k}} + \Omega \sum_{\mathbf{Q}} b_{\mathbf{Q}}^{\dagger} b_{\mathbf{Q}} + \sum_{\mathbf{k}, \mathbf{Q}} \frac{g_{\mathbf{Q}}}{\sqrt{N}} c_{\mathbf{k}-\mathbf{Q}}^{\dagger} c_{\mathbf{k}} (b_{\mathbf{Q}}^{\dagger} + b_{-\mathbf{Q}}). \quad (2)$$

The terms describe, in order, an electron with dispersion $\varepsilon_{\mathbf{k}}^b = -2t \sum_{i=1}^D \cos(k_i a)$ in D dimensions, an optical phonon with energy Ω and momentum \mathbf{Q} , and the

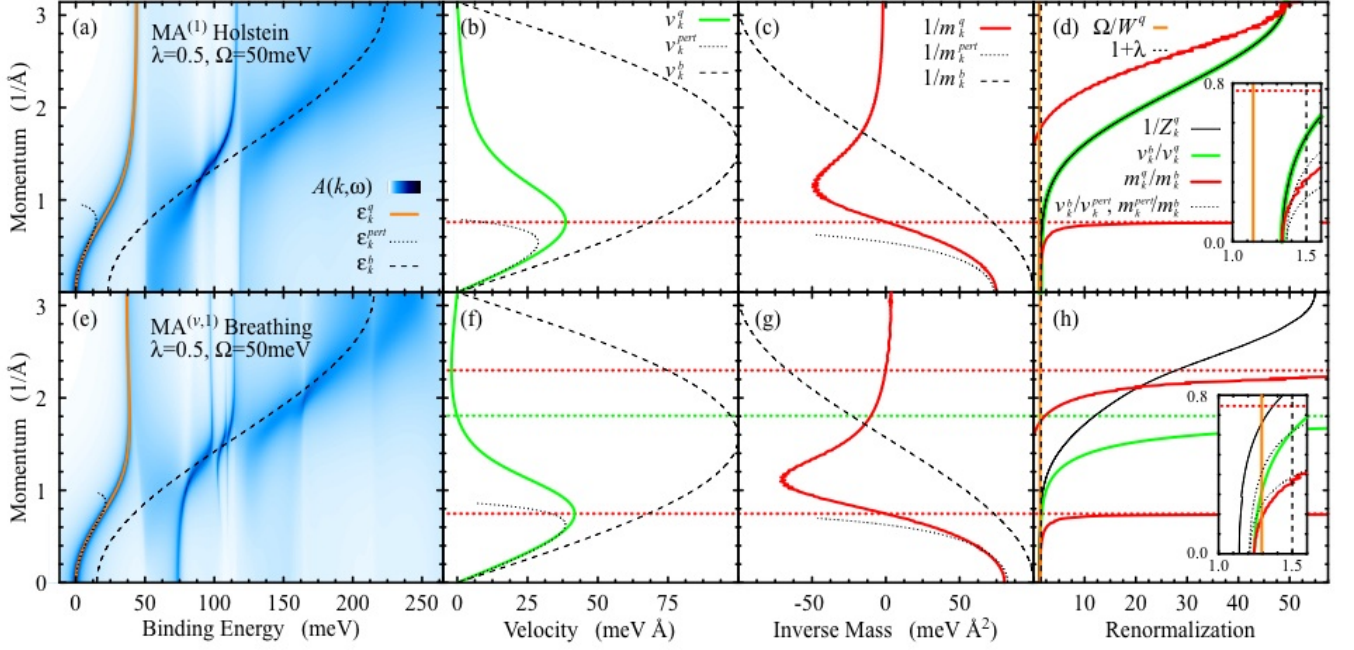


FIG. 2: (Color online). (a) $A(k, \omega)$ calculated for the momentum-independent Holstein self-energy in 1D with $MA^{(1)}$ for $\Omega = 50$ meV and $\lambda = 0.5$; the quasiparticle dispersion ε_k^q , perturbation theory (about $k = 0$) prediction ε_k^{pert} , and bare-band ε_k^b are also shown. (b) Quasiparticle (v_k^q), perturbation theory (v_k^{pert}), and bare-band (v_k^b) velocities, as well as (c) corresponding inverse masses, $1/m_k^q$, $1/m_k^{pert}$, and $1/m_k^b$ according to the definitions $v_k = \partial\varepsilon_k/\partial k$ and $1/m_k = \partial^2\varepsilon_k/\partial k^2$. (d) Momentum-dependent quasiparticle renormalization as obtained from v_k^b/v_k^q , m_k^q/m_k^b , as well as the inverse quasiparticle strength $1/Z_k^q$, where $Z_k^q = \int^q A(k, \omega)d\omega$ is the quasiparticle-only integrated spectral weight; in the inset, these quantities are compared near $k=0$ to the renormalization factors Ω/W^q and $(1+\lambda)$, obtained from quasiparticle bandwidth W^q (defined as the energy difference between top and bottom of the quasiparticle band) and dimensionless coupling $\lambda = g^2/2t\Omega$ as well as the perturbation theory prediction for mass and velocity renormalizations (shown with the same line style, but which can be distinguished by their proximity to the quasiparticle curves). In subsequent figures (3, 4, 5) the quantity plotted is the effective coupling, λ_{eff} , which would be implied by these renormalizations in the Migdal limit, which simply amounts to subtracting 1 from the renormalization. (e-h) demonstrate similar traces for a momentum-dependent self-energy from coupling to a single breathing-mode in 1D, here $\lambda = \langle |g|^2 \rangle / 2t\Omega$ is the average of the coupling across the Brillouin Zone. The noise is due to the finite simulation grid and subsequent lineshape fitting; slight variations in peak position are enhanced by taking the derivative numerically and therefore most visible in m_k^q .

on-site momentum-dependent electron-phonon coupling $g_{\mathbf{Q}}$ [for N sites with periodic boundary conditions; $c_{\mathbf{k}}$ ($c_{\mathbf{k}}$) and $b_{\mathbf{k}}^\dagger$ ($b_{\mathbf{k}}$) are the usual electron and phonon creation (annihilation) operators]. For the Holstein case $g_{\mathbf{Q}} \equiv g$ is a constant, leading to a dimensionless coupling $\lambda \equiv g^2/2Dt\Omega$, the ratio between lattice deformation energy $-g^2/\Omega$ and free-electron ground state energy $-2Dt$. For the breathing-mode $g_{\mathbf{Q}} \equiv -i\sqrt{2}g \sum_{i=1}^D \sin(Q_i a/2)$, which has an average value of $\langle |g_{\mathbf{Q}}|^2 \rangle = g^2$ across the Brillouin zone, allowing us to keep the same dimensionless coupling [49]. For this paper we set $a = \hbar = 1$ and $t = 50$ meV, such that the 1D bandwidth is 200 meV and the Brillouin zone is $2\pi\text{\AA}^{-1}$ wide. Also note that an additional constant 1 meV FWHM Lorentzian broadening is used, similar to an impurity scattering, to allow the numerical resolution of the sharpest features in $A(k, \omega)$.

The spectral function calculated with $MA^{(1)}$ for the Holstein problem in 1D with $\Omega = 50$ meV and

$\lambda = 0.1, 0.5, 1.0$ is presented as a false color plot in Fig. 1(a,b,c), along with the path of peak maxima measured through MDCs [$k_m(\omega)$] and EDCs (ε_k^q) compared with the bare-band dispersion ε_k^b . In the bottom panels (d,e,f) of Fig. 1 we present the real, $\Sigma'(\omega)$, and imaginary, $\Sigma''(\omega)$, parts of the self-energy for this momentum-independent model. Here each ε_k^q is a true (and the lowest) pole of the Green's function (it has zero width, hence an infinite lifetime), and is only resolved numerically owing to the impurity scattering inserted in the energy direction. One can see from Eq. 1 that the peak width should go roughly like $\Sigma''(k, \omega)$, and it is reassuring to see in Fig. 1(d,e,f) that the imaginary part of the self-energy is indeed zero near ε_k^q . The pole structure ε_k^q is also distinct from that of k_m , the path of peak maxima observed during MDC analysis; not only are they fundamentally different (as one is a function of ω and the other of k), but the path of peak maxima observed when cut-

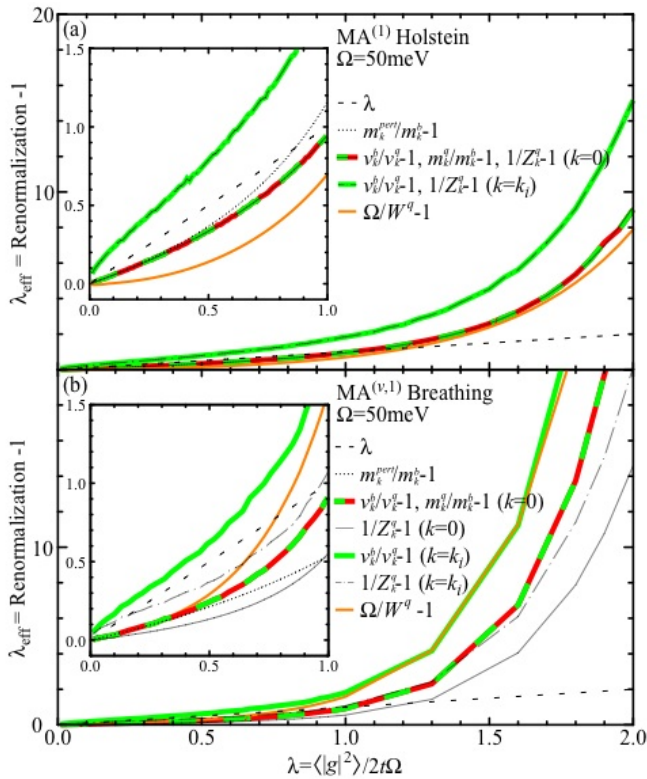


FIG. 3: (Color online). Effective coupling, λ_{eff} (as would be interpreted in the Migdal limit from the renormalization parameters defined as in Fig. 2), plotted vs. the true dimensionless coupling $\lambda = \langle |g|^2 \rangle / 2t\Omega$; where g is a constant for the Holstein model (a), and $g_Q \equiv -i\sqrt{2}g\sin(Qa/2)$ for the breathing-mode model (b). Also shown, in the inset only, are the predictions for observed effective coupling found via the mass renormalizations in perturbation theory (Eqs. 3 and 4) for the low-coupling regime at $k = 0$. Note that the noise in v and $1/Z$ at $k = k_i$ originates from the numerical determination of the inflection point k_i .

ting $A(k, \omega)$ in energy vs. momentum will not necessarily overlap, as has already been noted [4, 35].

For small couplings [Fig. 1 panel (a)] most of the spectral weight remains along ε_k^b , with only a small feature formed at energy Ω below the top of the band. With experimental resolution such a feature might appear only as a “kink” in a quasiparticle dispersion, however from looking at the self-energy [panel (d)] one can see that a distinction between ε_k^b and $k_m(\omega)$ should be made at this feature. The lowest pole, where $\Sigma''(\omega) \approx 0$ and which we will identify as the quasiparticle, only exists between the top of the band and Ω . This pole forms a narrow dispersion, ε_k^q , of bandwidth approximately Ω , although for k near the zone edge the electron spectral weight is very weak due to it having significant phonon character. The $k_m(\omega)$ path of MDC peak maxima, however, does not follow this quasiparticle dispersion but instead carries on close to the original bare-band ε_k^b into what we will identify as the continuum due to its broader structure and

finite Σ'' .

As the coupling is increased [Fig. 1 panels (b,c)], this distinction becomes increasingly more evident; the quasiparticle band gains spectral weight toward the zone boundary and becomes more well defined. Also its bandwidth narrows, becoming less than Ω as the quasiparticle mass increases and the quasiparticle velocity decreases. At the same time the spectral weight in the continuum becomes more spread out at deep energies, and new quasiparticle-like features begin to appear at the top of the continuum. At very large coupling (not shown) these additional features and the quasiparticle will eventually form a ladder of states with flat dispersions, although this coupling regime is well beyond the scope of this paper.

QUASIPARTICLE ANALYSIS

As can be visualized from Fig. 1, quasiparticle renormalizations do increase as the microscopic coupling increases. This monotonicity has led to widespread acceptance of measuring coupling through the quasiparticle mass, velocity or strength renormalizations observed with ARPES, often without reference as to whether or not the system should be expected to fall in the Migdal/Eliashberg framework. In this section we use our simple models to demonstrate that this scheme is not universal, and to make other observations, by performing quasiparticle analysis as is typically done with ARPES data (Fig. 2) on ~ 1200 generated spectral functions. These allow us to explore a wide range of couplings (Fig. 3), parameters (Fig. 4), and different dimensionality (Fig. 5) on models which provide both momentum-dependent and momentum-independent self-energies. Following a discussion of these results we will follow the mass renormalization behavior as $\lambda \rightarrow 0$ for $\mathbf{k} \sim 0$ in detail through perturbation theory (see Fig. 6 and Eqs. 3 and 4), the predictions for which are also plotted in Figs. 2 and 3 for comparison.

In order to perform quasiparticle analysis we generate an entire spectral function for each combination of the parameters: model, dimensionless coupling $\lambda = \langle |g|^2 \rangle / 2Dt\Omega$, phonon energy scale $\Omega/2t$, dimensionality D , and (for 2 and 3D) the desired cut through momentum space. For all simulations the form of the bare band is not changed and the hopping is set to a constant of $t = 50\text{meV}$ to give physically familiar values, a bandwidth of 200meV in the 1D case. (To consider other bandwidths one should simply scale the bandwidth, phonon energy, and coupling together as seen in the Hamiltonian, Eq. 2). On each of the ~ 1200 generated spectral functions the quasiparticle dispersion is found by fitting a Lorentzian peak with linear background to each EDC within the quasiparticle regime. The inclusion of a linear background allows the exclusion of any spectral

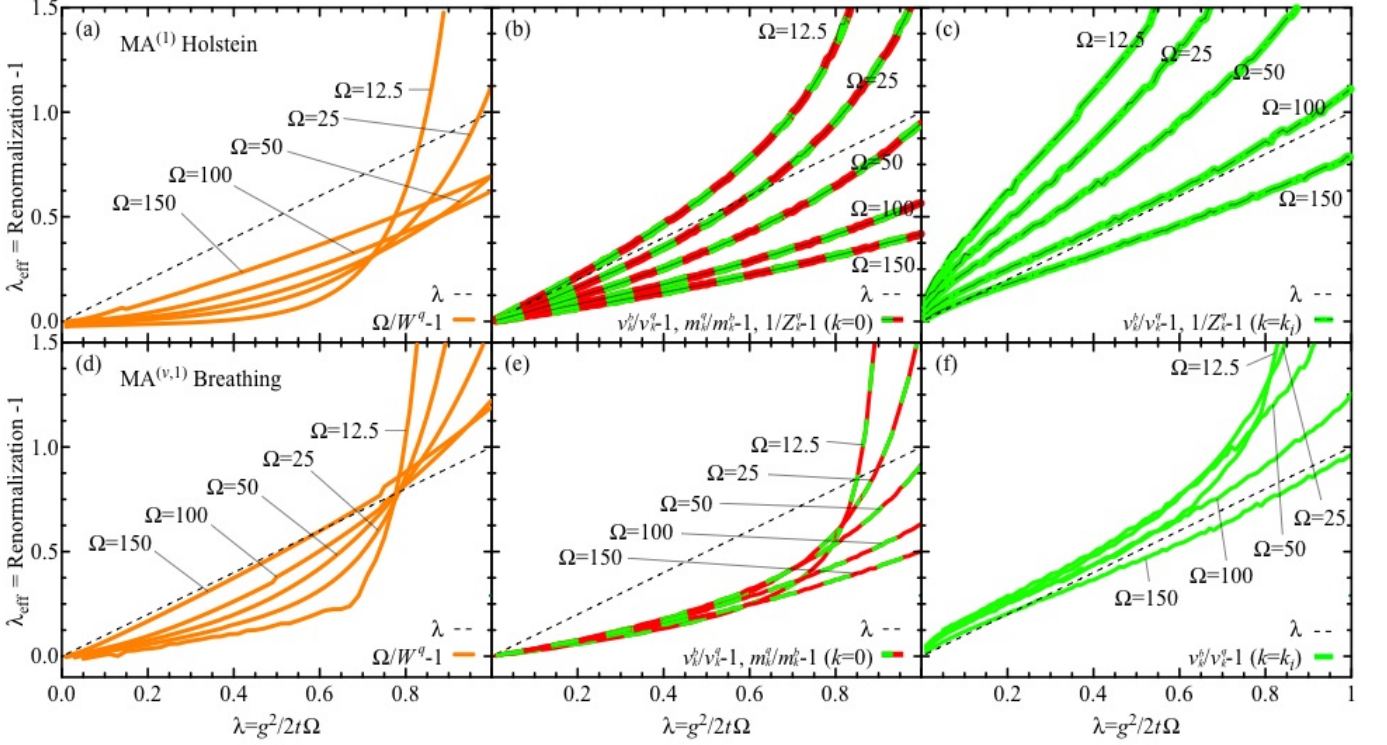


FIG. 4: (Color online). Effective coupling, λ_{eff} , (as would be interpreted in the Migdal limit from the renormalization parameters defined in Fig. 2) from the Holstein model (a-c) and breathing-mode model (d-f) plotted vs. the true dimensionless coupling $\lambda = g^2/2t\Omega$ for a range of phonon energies Ω labelled in meV. In panels (b, c) those from multiple renormalization parameters (which lie directly on top of each other) are all plotted, whereas in (e, f) those from inverse quasiparticle weight do not fall on any other curve and are therefore omitted for clarity. The slope at $\lambda = 0$ in panels (b, e) is the quantity plotted in Fig. 6. Note that the noise in panels (c, f) originates mostly from the numerical determination of the inflection point k_i , while in (a, d) it stems mostly from variations fitting the quasiparticle peak location at high momentum where it has less weight.

weight from the continuum which bleeds in (a problem especially at low couplings and high dimensions). We illustrate this analysis in Fig. 2, where we present the spectral function $A(k, \omega)$ for a mid-range coupling $\lambda = 0.5$ and phonon energy $\Omega = 50$ meV for both the Holstein and breathing-mode models as well as dispersions found from the Lorentzian fits ε_k^q , perturbation theory prediction $\varepsilon_k^{\text{pert}}$, and the bare electronic structure ε_k^b [panels (a,e)]. Also shown are the velocities [v_k^q , v_k^{pert} and v_k^b in panels (b,f)], inverse masses [$1/m_k^q$, $1/m_k^{\text{pert}}$ and $1/m_k^b$ in panels (c,g)], the corresponding renormalization ratios v_k^b/v_k^q , m_k^q/m_k^b and their perturbation theory predictions, along with the inverse quasiparticle strength $1/Z_k^q$ and bandwidth renormalization Ω/W^q [panels (d,h), see caption for definitions]. In Fig. 2 panels (a-d) present the results for the Holstein model (with a momentum-independent self-energy), while panels (e-h) refer to the breathing-mode coupling (with a momentum-dependent self-energy).

Fig. 2 (d,h) show that the velocity, mass, and spectral weight renormalizations are all functions of momentum, which raises concerns if one would compare them to the bandwidth renormalization Ω/W^q , or an ‘expected’

renormalization factor of $(1 + \lambda)$ which are both constant. Although they do cross at certain values of k this is merely accidental, and none match at the top of the band - our ‘Fermi surface’. More problematic is that the mass renormalization must necessarily contain a divergence if the inflection point of ε_k^b is different from ε_k^q , where $1/m_k^q$ vanishes (emphasized by the horizontal dashed line). Similarly, in the case of momentum-dependent coupling [panels (e-h)], it can be seen that the quasiparticle dispersion ε_k^q is not even monotonic, causing another divergence when v_k^q vanishes in the middle of the dispersion (this non-monotonic dispersion is a direct consequence of the structure of the polaronic cloud, which causes a larger second-nearest-neighbour hopping, and is discussed at length in Ref. 36). Due to this momentum-dependence, any estimation of λ drawn from v_k^b/v_k^q , m_k^q/m_k^b , or $1/Z_k^q$ would depend heavily on the momentum chosen; and if either of v_k^b/v_k^q or m_k^q/m_k^b were used close to their divergences, the estimated value could be off by an unlimited amount. Even Ω/W^q , although constant in k , does not match the value of $(1 + \lambda)$ for either the momentum-independent or momentum-dependent case. From Fig. 2 we draw the conclusion that none of the renormalization

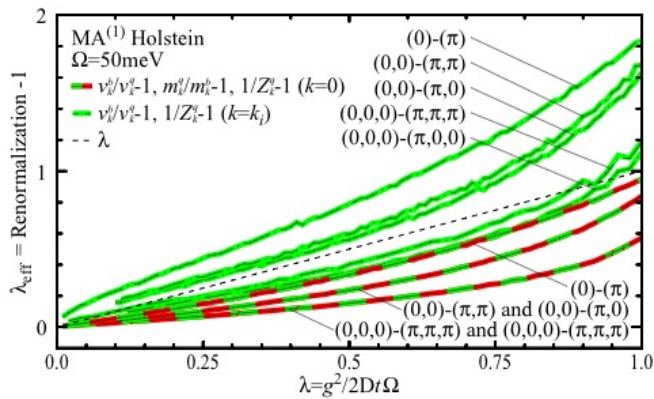


FIG. 5: (Color online). Effective coupling, λ_{eff} , (as would be interpreted in the Migdal limit from the mass and velocity renormalization parameters defined in Fig. 2) from the Holstein model and plotted vs. the true dimensionless coupling $\lambda = g^2/2Dt\Omega$ for different dimensionalities and high-symmetry cuts. Note that the noise in v and $1/Z$ at $k = k_i$ originates from the numerical determination of the inflection point k_i .

quantities gives a good direct estimate of the dimensionless coupling $\lambda = \langle |g^2| \rangle / 2t\Omega$. Further we find that, with the exception of the quasiparticle strength and velocity renormalization in the Holstein model only (which we will return to), the renormalizations do not match even each other - even though the models were kept as similar and simple as possible. This indicates that making even qualitative comparisons of ‘coupling’ from experiments on different materials (or even different experiments on the same material) through these renormalization parameters may not be meaningful. However, modelling of the parameters in question from the original Hamiltonian via perturbation theory might be a start, as these results show much closer agreement near $k = 0$ despite the relatively high (for perturbation theory) coupling (we will return to discuss perturbation theory later).

Despite their differences from each other and their momentum dependence, however, these renormalizations do monotonically increase as the microscopic coupling increases (as previously observed in Fig. 1) which naturally leads one to wonder how, precisely, these quantities scale with λ as well as Ω in our different models, so that one might be able to capture the trend if the material and measured quantity is held constant - for example, if that doping does not cause structural distortions. In Fig. 3 we will follow the ‘effective coupling’, λ_{eff} (which is simply the observed renormalization minus 1), that each of these renormalization quantities would predict using the Migdal/Eliashberg framework as a function of λ , as well as renormalizations found using the perturbation theory results around $k = 0$ (Eqs. 3 and 4), for both momentum-independent [panel (a)] and momentum-dependent [panel (b)] self-energies. In Fig. 4 we plot a selection of these quantities in the same fashion, for a range of phonon en-

ergies. For the momentum-dependent quantities we must choose a k value: we plot v_0^b/v_0^q , m_0^q/m_0^b , and $1/Z_0^q$ at $k = 0$ (our ‘Fermi surface’), as well as $v_{k_i}^b/v_{k_i}^q$ and $1/Z_{k_i}^q$ at the inflection point $k = k_i$ of the quasiparticle band ε_k^q , where $m_{k_i}^q/m_{k_i}^b$ diverges.

In Fig. 3 we find that the predictions from all quantities scale monotonically with the microscopic coupling and are concave up. In the low coupling regime (below about $\lambda = 0.3$) the perturbation theory results match the simulations - however nowhere does λ_{eff} match λ from the Hamiltonian. At small coupling values, using this model, many renormalization quantities would drastically underestimate the true microscopic coupling, by a factor ranging from infinite (Ω/W near $\lambda = 0$ where it is not renormalized in the Holstein model) to ~ 6 ($1/Z_{k_i}^q$ near $\lambda = 0.1$, breathing-mode). Conversely, at larger coupling values ($\lambda \sim 2$) all quantities would overestimate the true microscopic coupling, with factors ranging from ~ 4 (Ω/W , Holstein) to ~ 22 ($v_{k_i}^b/v_{k_i}^q$, breathing-mode). We also find that, depending on the coupling or model, the relative renormalization strength of quantities changes - for the momentum-independent model Ω/W is renormalized the least, whereas in the momentum-dependent model $1/Z_0^q$ shows the least renormalization. This indicates, yet again, that comparing different materials via renormalizations is not feasible, nor is comparing different renormalizations on the same material without a detailed model. We note again that, in the Holstein model only, quasiparticle strength and velocity renormalization are identical for all couplings at both $k = 0$ and $k = k_i$ (as previously seen in Fig. 2 where they are identical at all momenta).

In Fig. 4 we follow the same quantities for a variety of phonon energies, allowing Ω to vary from $1/16$ to $3/4$ of the bare-band width for both models (although inverse quasiparticle weight is omitted from the breathing-mode plots for clarity). First we note that there are some qualitative similarities, but just as many differences. In all these 1D cases the concavity increases as phonon energy decreases, so that by the mid-coupling regime ($\lambda \approx 1$) we recover the expected dependence - phonons which are easier to excite (require less energy) renormalize the band more. However, in the low coupling regime we do not find this dependence (later seen again in Fig. 6 and in agreement with Eqs. 3 and 4). For both models the bandwidth [panels (a, d)] shows the opposite behavior for low coupling, with a transition near $\lambda = 0.8$. Still considering the low-coupling regime, mass and velocity renormalizations show little dependence on the phonon energy for the breathing-mode model, yet strong dependence in the Holstein case. Again we find that the renormalizations and their corresponding ‘effective couplings’ vary widely from each other, and depend on the model and parameters chosen - sometimes in counterintuitive ways.

The final parameter to be varied is dimensionality, which we explore briefly with Fig. 5 for the Holstein

Hamiltonian in the low coupling regime only. Here we find that for a fixed dimensionality and phonon energy where $\Omega \sim t$ the renormalizations as a function of λ look qualitatively similar. The various renormalized quantities increase monotonically yet remain distinct from the microscopic coupling as well as each other (with the exception of quasiparticle strength and velocity renormalization which are again the same), with details that depend on phonon energy and dimensionality. We feel it is important to note, however, that at larger couplings not explored here other studies on the dynamics of the Holstein (and momentum dependent Su-Schrieffer-Heeger) models have found more complicated behavior in higher dimensions; where a critical coupling value marks a drastic change in quasiparticle properties, which is most prominent as $\Omega \rightarrow 0$ [37–40]. However interesting, this type of behavior would not simplify quasiparticle renormalization analysis on such a system and is not investigated here.

So far we have shown that, while the slope may not be 1, the renormalization curves could all still be reasonably well approximated as *linear* in λ in the very low coupling regime and that perturbation theory makes an excellent prediction for them near $k = 0$. This allows us to follow this slope more continuously through parameter space with perturbation theory than by simulating even larger numbers of spectral functions. It is worth noting that in the classic implementation of the $(1 + \lambda)$ scheme (see Ref. 7), perturbation theory is discussed but dismissed as a possible avenue due to the resulting corrections being too large for perturbation theory to be valid. However, in that instance, some approximations are made to ease completion of the integrals which eliminate the possibility of the arbitrarily small couplings we have used here. In our case the lowest non-zero order in the phonon-electron interaction term from Eq. 2 is the second, and in 1D we find that for both models it is possible to complete the integrals without further approximation. In the Holstein case the energy dispersion should be modified from $\varepsilon_k^b = -2t\cos(ka)$ to:

$$\varepsilon_k^{pert} \approx -2t \left(\cos(ka) + \lambda \frac{\frac{\Omega}{2t}}{\sqrt{(\cos(ka) + \frac{\Omega}{2t})^2 - 1}} \right), \quad (3)$$

which agrees with the results calculated for the quasiparticle residue at $k = 0$ in Ref. 41. For the breathing-mode model we find that the dispersion becomes:

$$\varepsilon_k^{pert} \approx -2t \left(\cos(ka) + \lambda \frac{\Omega}{2t} \mathcal{F} \left(\frac{\Omega}{2t}, k \right) \right)$$

$$\mathcal{F} \left(\frac{\Omega}{2t}, k \right) \equiv \cos(ka) + \frac{\sin^2(ka) - \frac{\Omega}{2t} \cos(ka)}{\sqrt{(\cos(ka) + \frac{\Omega}{2t})^2 - 1}}. \quad (4)$$

This demonstrates that, at the very least, we should not expect the renormalizations to depend solely on the

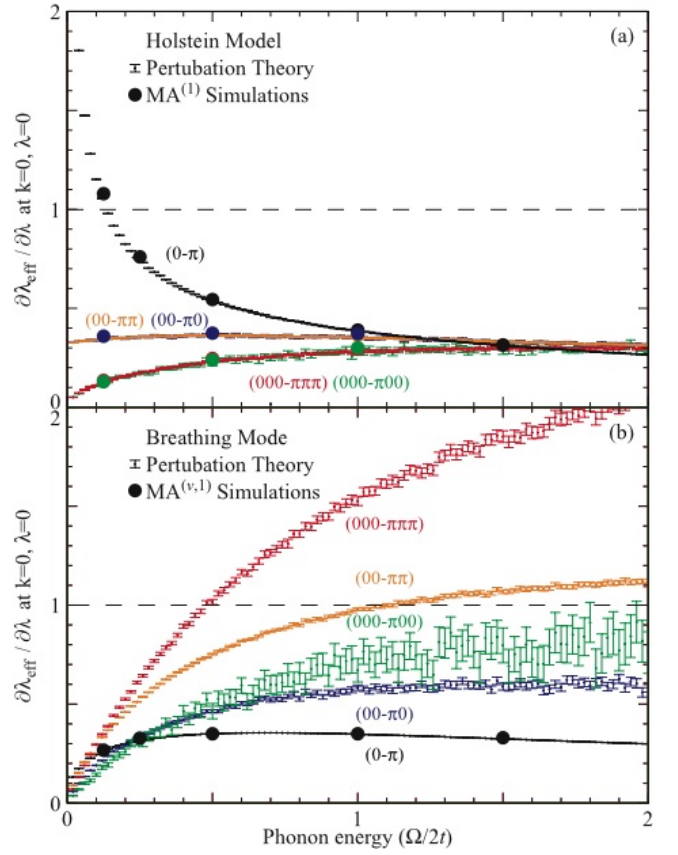


FIG. 6: (Color online). Rate of change in observed effective coupling, λ_{eff} , per change in true dimensionless coupling, λ , defined as $\partial \lambda_{\text{eff}} / \partial \lambda|_{k=0, \lambda=0}$ (where $\lambda_{\text{eff}} \equiv m_k^a / m_k^b - 1$ is as predicted by perturbation theory and measured from simulated spectral functions and $\lambda = \langle |g|^2 \rangle / 2Dt\Omega$) plotted as a function of the phonon energy for (a) Holstein model and (b) coupling to a breathing mode. If the Migdal limit holds this derivative would be a constant, 1, for all values of $\Omega/2t$. For $D > 1$ cuts from the Γ point to both the corner and face of the Brillouin Zone were considered, as labelled. Vertical error in the results from simulated spectral functions is comparable to symbol size and results from approximating the slope at $\lambda = 0$ from the finite data points in Figs. 4 and 5, as well as similar simulation sets not shown. Uncertainty in the perturbation theory results stems from the numeric Monte Carlo integration used to determine the perturbation energies, taken from the distribution of independent subsets of total points evaluated, and is higher for non-diagonal cuts due to the narrower bandwidth in that direction. The curves predicted by Ref. 37 for the Holstein Model in 1 and 2 dimensions are not shown as they would be hidden by symbols, but fall exactly onto the perturbation theory results.

dimensionless coupling $\lambda = g^2/2t\Omega$, but also on the other relevant energy scale in the problem - the ratio of phonon energy to bandwidth. By taking derivatives of these dispersions we can also find the predicted mass and velocity renormalizations. In Fig. 2 we plot the predicted dispersion, derivatives, and renormalizations contrasted against the simulated spectral function and find close but not

perfect agreement for both models near $k = 0$ (but failing at large momenta), despite the relatively high coupling ($\lambda = 0.5$). As seen in Figs. 3 and 6 near $k = 0$ for vanishing λ there is perfect agreement within our measurement accuracy; perturbation theory begins to show signs of failure near $\lambda \approx 0.25$. In higher dimensions we did not complete the integrals exactly but instead used the VEGAS Monte Carlo integration algorithm to evaluate them numerically [42–44]. Using this routine for all dimensionalities allowed us to validate the results by comparing them to these known solutions for 1D for both models and the results found in Refs. 37, 41 for the Holstein model in 1 and 2D, where they show perfect agreement (once corrected for a slightly different definition of λ in 2D).

In Fig. 6 we show how the renormalization with the dimensionless coupling parameter λ near $k = 0$, $\lambda = 0$ (and hence the observed effective coupling, λ_{eff}) varies as a function of the other energy scale $\Omega/2t$ for both models in 1, 2 and 3 dimensions, and how this matches nearly perfectly against measurements of the same quantity on the simulations. Interestingly, despite spectral functions which have outwardly similar characteristics [as seen, for example, in Fig. 2 panels (a vs. e) or Fig. 10 vs. Fig. 8], we find a drastic difference in how the actual renormalizations vary with phonon energy depending on the model, and that neither model would be well approximated by a $\lambda_{\text{eff}} = \lambda$ scheme, which is shown as the dashed line along 1. The 1D Holstein model shows a perhaps expected dependence: phonons which require very little energy to excite have a dramatic effect on the electronic renormalization (blowing up as $\Omega \rightarrow 0$); but as the phonon energy increases, the mode has progressively less effect. In the 2D case, however, we find very limited dependence on phonon energy with a curve that is almost flat and could therefore be rescaled to match if λ was chosen to be defined appropriately. In 3D we find the opposite of the 1D case whereby the renormalization vanishes as $\Omega \rightarrow 0$. These very different limits are directly related to the bare-electron DOS at the band-edge, and its strong dependence on dimensionality [37]. In all dimensions we find that the renormalization is isotropic (as one might expect from an isotropic coupling) and that it asymptotically approaches a similar value for large phonon energies - reminiscent of a renormalization which depends solely on λ , if only for $\Omega/2t \gg 1$. In stark contrast, however, the more realistic breathing-mode model shows entirely different behavior. For all dimensionalities the overall functional form is similar for $\Omega \rightarrow 0$, where mass renormalizations vanish. This low energy behavior may be expected as for weak coupling and energies close to $k = 0$ in the bare-band, the electron couples mostly to $q \approx 0$ phonons; and in this model such coupling vanishes, $g(q \rightarrow 0) \rightarrow 0$. As the phonon energy increases, however, we discover that the renormalization is anisotropic with stronger renormalization along the diagonal cut (as may

be expected for an anisotropic coupling) and a coupling which gets stronger as dimensionality increases (opposite the Holstein case). We also find that the renormalizations do not asymptotically approach any fixed value for large phonon energies, as they did for the Holstein case.

Overall we find that there is much variability in quasiparticle analysis, to the point that one cannot make a general rule about renormalizations in this regime. There are, however, two common threads. Firstly, for both our models, perturbation theory works in the low coupling regime: it correctly predicts the quasiparticle band structure near $k = 0$ for all combinations of parameters tested, although it fails at higher momenta (as seen in Fig. 2). The second, and perhaps more interesting, hints at something which may be quantitatively gained through quasiparticle analysis - without even a more detailed model on which to attempt perturbation theory or other tools. In Figs. 2, 3, 4, and 5 one observes that, in the momentum-independent case only, v_k^b/v_k^q and $1/Z_k^q$ lie precisely on top of each other for all values, and match m_k^q/m_k^b at $k = 0$. Although the velocity and mass renormalizations at $k = 0$ are simply a consequence of derivatives following each other near an extremum, the velocity renormalization and quasiparticle strength have implications for the structure of the self-energy, as was previously noted in Ref. 20 and is discussed in greater detail now.

By definition, the Green's function is:

$$G(k, \omega) = \frac{1}{\omega - \varepsilon_k^b - \Sigma(k, \omega) + i\eta}. \quad (5)$$

In the infinite lifetime quasiparticle regime the self-energy should be purely real, with any broadening coming solely from the small impurity scattering, η . We may then identify the implicitly defined quasiparticle dispersion as $\varepsilon_k^q = \varepsilon_k^b + \Sigma(k, \omega)|_{\omega=\varepsilon_k^q}$ and, since we are interested in an EDC, expand the self-energy about $\omega = \varepsilon_k^q$ to first-order in energy. Taking $-1/\pi$ times the imaginary part yields the spectral function:

$$A(k, \omega) \approx \frac{1}{\pi} \frac{\eta}{\eta^2 + (\omega - \varepsilon_k^q)^2 \left(1 - \frac{\partial \Sigma(k, \omega)}{\partial \omega} \Big|_{\omega=\varepsilon_k^q}\right)^2}. \quad (6)$$

We can see that, cut along energy in the quasiparticle regime, the spectral function will be a Lorentzian at ε_k^q with width given by η and with weight $Z_k = 1/(1 - \frac{\partial \Sigma(k, \omega)}{\partial \omega} \Big|_{\omega=\varepsilon_k^q})$. This relationship between quasiparticle weight and the energy derivative of the self-energy is often derived, and usually associated directly with the success of an effective coupling scheme [6, 7], but we do *not* make that association here. Velocity renormalization is simply the ratio of momentum derivatives of the bare, v_k^b , and quasiparticle $v_k^q = v_k^b + \frac{\partial \Sigma(k, \omega)}{\partial \omega} \Big|_{\omega=\varepsilon_k^q} v_k^q + \frac{\partial \Sigma(k, \varepsilon_k^q)}{\partial k}$ bands, which reduces to:

$$\frac{v_k^b}{v_k^q} = \frac{1}{Z_k} - \frac{\partial \Sigma(k, \varepsilon_k^q)}{\partial k} \frac{1}{v_k^q}. \quad (7)$$

We see that, for momentum-independent self-energies, the velocity renormalization must follow the inverse spectral weight. This means that the renormalization quantities can be used to conclusively check the momentum-dependence of the self-energy, in the quasiparticle regime. Whether or not the self-energy is momentum-dependent is of great importance to MDC self-energy analysis, on which we focus in the rest of the paper.

SELF-ENERGY ANALYSIS

Since quasiparticle analysis fails to reveal the true microscopic coupling through renormalizations, we look toward other options for spectral function analysis. In this section we describe how it is possible to estimate the self-energy through the analysis of MDC lineshapes. We will begin, for simplicity, with a description for momentum-independent self-energy and move on to describe the implications of momentum-dependence on the procedure. Cases of a momentum-independent self-energy can be verified through quasiparticle analysis; as seen in Eq. 7 the *overlap* of v_k^b/v_k^q and $1/Z_k^q$ is only possible when the self-energy is *momentum-independent* along the quasiparticle dispersion. Although the quasiparticle dispersion and the path of MDC peak maxima where MDC analysis is carried out may vary, in practice they are often very close in the quasiparticle regime. One must always keep in mind that although a momentum-independent self-energy causes a Lorentzian MDC lineshape, Lorentzian lineshape alone is not sufficient to conclude that $\Sigma(k, \omega) = \Sigma(\omega)$ [26].

In cases where the self-energy is momentum-independent we may analyze $A(k, \omega)$ in terms of MDCs at constant energy $\omega = \tilde{\omega}$, where the self-energy may then also be considered a constant. Under this condition, as long as ε_k^b can be linearized in the vicinity of the MDC peak maximum observed at $k = k_m$, the MDC lineshape will be Lorentzian. By Taylor expanding ε_k^b about an MDC peak maximum at $k = k_m$, i.e. $\varepsilon_k^b = \varepsilon_{k_m}^b + v_{k_m}^b \cdot (k - k_m) + \dots$, ignoring higher order terms (which must be negligible if the curve appears Lorentzian), and noticing that $\varepsilon_{k_m}^b + \Sigma'_{\tilde{\omega}} - \tilde{\omega} = 0$ will implicitly define the observed peak maximum, we can rewrite Eq. 1 as:

$$A_{\tilde{\omega}}(k) \simeq \frac{A_0}{\pi} \frac{\Delta k_m}{(k - k_m)^2 + (\Delta k_m)^2}, \quad (8)$$

with:

$$\begin{aligned} \Delta k_m &= -\Sigma''_{\tilde{\omega}}/v_{k_m}^b = \text{HWHM}, \\ A_0 &= 1/v_{k_m}^b = \int A_{\tilde{\omega}}(k) dk. \end{aligned} \quad (9)$$

Here Δk_m is the half-width half-maximum (HWHM) of a Lorentzian of weight A_0 . For each constant energy cut,

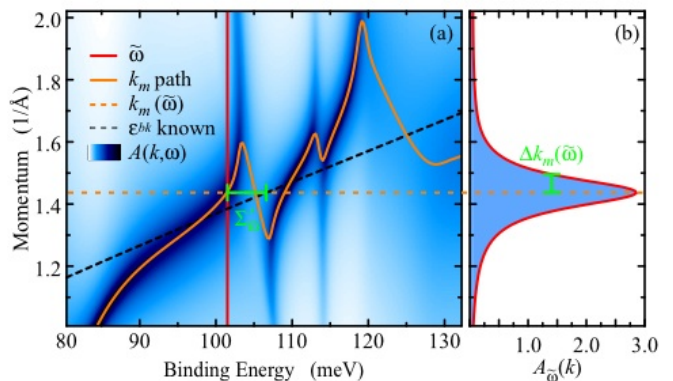


FIG. 7: (Color online). Eq. 8 and Eq. 10 described diagrammatically for a momentum independent self-energy. (a) is a false color plot with the bare-band (ε_k^b) and path of peak maxima (k_m path) shown in addition to an example MDC cut at $\tilde{\omega}$ and the peak maximum location for that cut [$k_m(\tilde{\omega})$]. (b) the cut through momentum of $A(k, \omega)$ at constant energy $\tilde{\omega}$, observed to be a Lorentzian with a peak maximum located at $k_m(\tilde{\omega})$, a HWHM $\Delta k_m(\tilde{\omega})$, and an area $A_0(\tilde{\omega})$. These lineshape properties are related to the self-energy at $\tilde{\omega}$ through the bare-band evaluated at k_m through Eq. 10

$\omega = \tilde{\omega}$, the observed peak maximum is labelled k_m . The self-energies are then easily found as:

$$\begin{aligned} \Sigma'_{\tilde{\omega}} &= \tilde{\omega} - \varepsilon_{k_m}^b, \\ \Sigma''_{\tilde{\omega}} &= -\Delta k_m v_{k_m}^b. \end{aligned} \quad (10)$$

One must be careful visualizing the relationships; although a simple picture might be that the peak, whose width scales with the imaginary self-energy and band velocity, has been ‘pushed up’ by the real self-energy to its observed location at $\tilde{\omega}$, one must remember that these quantities are defined implicitly and evaluated at different locations in the (k, ω) plane: the self-energy is evaluated at $(k_m, \tilde{\omega})$ and the bare-band at $(k_m, \varepsilon_{k_m}^b)$. Of course, these implicit definitions are no trouble if you simply wish to *observe* $A(k, \omega)$ and not *calculate* it based on this simple approximation. These relations are illustrated graphically in Fig. 7.

These relationships work exactly where they are applicable: namely when the self-energy is momentum independent, k_m is far from a band edge (where $v_{k_m}^b$ must vanish), where the peak shape is truly Lorentzian, and when the peak width is narrow enough that a first-order expansion of ε_k^b is appropriate. Since the convolution of two Lorentzians is another Lorentzian where the peak width is a simple sum of the widths of the original functions, the inserted impurity scattering shows up directly as an addition to the measured $\Sigma''_{\tilde{\omega}}$ (for comparison purposes a constant $\eta = 1$ meV has therefore been subtracted from all plots of $\Sigma''_{\tilde{\omega}}$). However, these relationships still hinge on knowledge of the bare-band. If ε_k^b is unknown it is possible to fit it, to within an arbitrary energy offset, to any functional form which provides a value and derivative

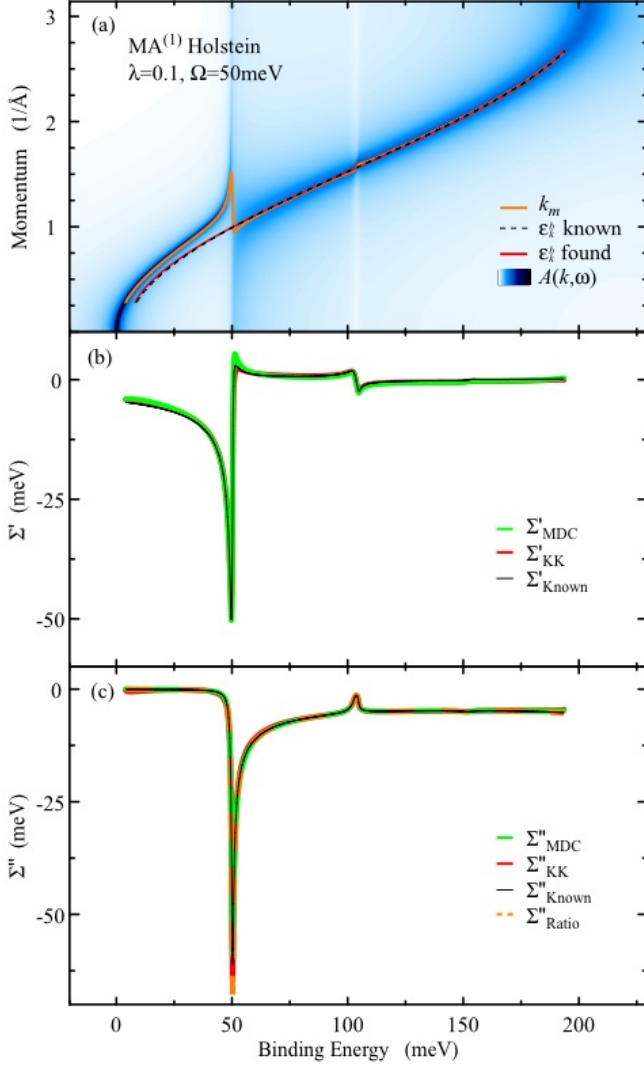


FIG. 8: (Color online). (a) $A(k, \omega)$ calculated for the momentum-independent Holstein self-energy with MA⁽¹⁾ for $\Omega = 50$ meV and $\lambda = 0.1$ as a false color plot; also shown are the k_m path of MDC maxima along which the analysis is performed, as well as the known bare-band and the third order polynomial approximation found through the KKBF analysis (the arbitrary energy offset introduced through KKBF has been shifted back by hand to allow comparison between the two). (b,c) Real and imaginary parts of the self-energy from the model (Σ_{known}), the bare-band and MDC fitting routine (Σ_{MDC}) as found via Eq. 10, and the KK transform of Σ_{MDC} (Σ_{KK}) and Σ'_{MDC} (Σ''_{KK}) used as an internal check in KKBF. In (c) the MDC ratio results, Σ''_{ratio} , as found via Eq. 11 are also shown.

using a Kramers-Kronig bare-band fitting (KKBF) routine (see Appendix). Alternatively, as previously noted in Ref. 20 and used in Ref. 45, the imaginary part of the self-energy requires knowledge of only $v_{k_m}^b$, which can be obtained directly from $A_0 = 1/v_{k_m}^b$, allowing us to write it as the MDC width/integral ratio:

$$\Sigma''_{ratio} = -\Delta k_m / A_0 \quad (11)$$

This variation allows us to tackle the problem over a larger range of λ as it does not rely on the KKBF routine to succeed over the entire range in order to ensure the fitness of the Kramers-Kronig transform and fit the bare-band. Eq. 11 is free to work over energies where the peak is Lorentzian (i.e. Eq. 8 holds), and to fail in others without allowing these failures to block the procedure. Experimentally, when using this ratio, one must be careful that the observed spectra are properly normalized, otherwise it will be off by a constant multiple, but even if this is not possible the form of the imaginary self-energy should be nevertheless recoverable. It is also possible, in cases of momentum-independent self-energy for which $v_k^b/v_k^q = 1/Z_k^q$ from Eq. 7, to find the same ratio using only quasiparticle properties as $\Sigma''_{MDC} = -v_{k_m}^q \Delta k_m / Z_{k_m}^q$.

The results of both the KKBF and the ratio method, performed as if the bare-band was not known on a momentum-independent self-energy in the low-coupling regime, are presented in Fig. 8. The internal self-consistency of the KKBF results is confirmed by the good match between Σ_{MDC} and Σ_{KK} , and the agreement of Σ_{Ratio} adds further confidence. These ‘measured’ quantities show good agreement with their known counterparts everywhere Eq. 8 is applicable, demonstrating that these methods work well in the low-coupling regime; however, they become progressively less accurate as the coupling increases. In Fig. 9(a) we show the progressive failure of the method applied for couplings where λ ranges from 0-1, which demonstrates a rapid degeneration of the accuracy of the method outside of the low-coupling regime. Note, however, that the two methods fail in different ways. Σ''_{MDC} tends to fail more globally, whereas Σ''_{Ratio} often continues to work almost exactly in some energy regions while failing catastrophically in others (these regions cause its average deviation, shown in Fig. 9, to indicate perhaps a higher degree of failure than deserved). In Fig. 9(b) we demonstrate these differences by showing the results of the methods applied blindly at $\lambda = 0.5$, even though lineshapes show that there are areas where Eq. 8 does not apply. One can see how the internal KKBF check has begun to fail as Σ''_{MDC} and Σ''_{KK} do not match; there are structural differences and Σ''_{KK} has picked up different offsets in the different flatter parts of the spectrum, making setting its overall offset difficult. As the disagreement between Σ''_{MDC} and Σ''_{KK} increases with coupling it will eventually cause the KKBF routine to fail to capture the bare electronic structure. None of the methods reproduce Σ''_{Known} near the sharp one-phonon structure; note that Σ''_{MDC} and Σ''_{Ratio} overestimate and underestimate it, respectively. Our experience with this model leads us to believe this to be typical behavior: when each method fails they do not tend to fail in identical ways, so that in regions where they do match one can still have confidence that the methods are working.

These methods hinge on the momentum-independence of the self-energy in two ways. For fitting line-

shape, a momentum-independent self-energy guarantees a Lorentzian lineshape but the inverse is not true - it is still possible to have a momentum-dependent self-energy which generates a Lorentzian. Additionally, fitting the bare-band relies on the Kramers-Kronig transforms in energy, which are only valid for a fixed momentum. In cases where the momentum-dependence is not too strong locally near k_m , however, we have found that it is still possible to gain insight using similar approaches, although even more care must be taken in the interpretation of the results. If, despite momentum-dependence, the MDC appears Lorentzian in shape, certain higher order terms must be small when expanding each of ε_k^b , $\Sigma'(\omega, k)$ and $\Sigma''(\omega, k)$ about k_m . Under this condition we may drop terms of order $(k - k_m)^3$ and higher from the denominator as well as $(k - k_m)$ and higher from the numerator, which also implies we may drop $\partial\Sigma''/\partial k$ and $\partial^2\Sigma''/\partial k^2$ everywhere. We end up with an expression identical to Eq. 8, only with new interpretations for the HWHM as well as the spectral weight of the peak:

$$\Delta k_m = \frac{\Sigma''(\tilde{\omega}, k_m)}{v_{k_m}^b + \partial\Sigma'(\tilde{\omega}, k_m)/\partial k},$$

$$A_0 = \int A_{\tilde{\omega}}(k) dk = \frac{1}{v_{k_m}^b + \partial\Sigma'(\tilde{\omega}, k_m)/\partial k}. \quad (12)$$

Now that the self-energies are momentum-dependent it becomes more important to remember that the self-energy extracted using this method will follow the k_m path through (ω, k) space; this path is demonstrated as a false color plot in Fig. 10(d,e,i,j). From Eq. 12 we find that, in this momentum-dependent case, the ratio check Eq. 11 proves to be invaluable as it removes the possible inaccuracies when strong momentum-dependence near k_m in Σ' might provide a Lorentzian lineshape with a misleading width viewed from a momentum-independent perspective. In Fig. 10(a-c,f-h) we present the results of both KKBF and the ratio method for a momentum-dependent coupling. From a comparison between the measured and known self-energies on paths through k space along the zone boundaries and along k_m , we find agreement only along the k_m path, as expected. Further, especially in Fig. 10h near the 3rd phonon structure close to $\sim 125\text{meV}$, one can see how it is possible for Σ''_{MDC} and Σ''_{KK} to agree with each other and yet not correctly predict Σ''_{Known} , despite the peak shape being reasonably Lorentzian, due to sufficient local momentum-dependence in the real self-energy (Fig. 10i). In this location we note, however, that Σ''_{Ratio} still correctly predicts Σ''_{Known} as it is not affected by this local momentum-dependence. Overall we find that, in a similar fashion to the momentum-independent case, there is generally good agreement between the found self-energies and the self-energy along the k_m path in the low-coupling regime and the methods progressively fail

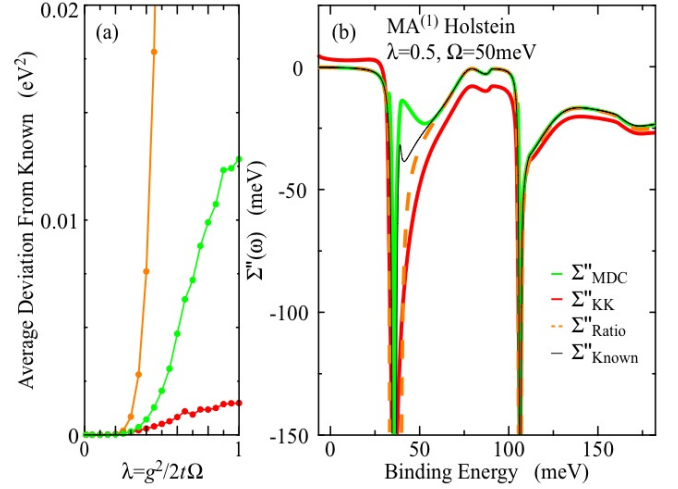


FIG. 9: (Color online). (a) Deviation (i.e., average of the squared difference at each k_m) between estimated and known self-energies vs. λ . (b) Various estimates for the imaginary part of the self-energy, defined as in the caption of Fig. 8, for $A(k, \omega)$ calculated within MA⁽¹⁾ for $\Omega = 50\text{meV}$ and $\lambda = 0.5$.

as we move into the mid-coupling regime. The available modes of failure are increased: there are more locations where the lineshape is not Lorentzian due to strong local momentum-dependence of the self-energy; places where it is still Lorentzian but with a misleading width; and the Kramers-Kronig relations are not valid along an arbitrary path through (ω, k) space, which disrupts the fitness of the KKBF routine. While it is not surprising that the KKBF routine eventually fails for large couplings in the momentum dependent case it is interesting that it works at all, as the Kramers-Kronig relations in energy are only formally valid for a fixed momentum but the measured self-energies follow the k_m path at all couplings. Despite this, as can be seen in Fig. 10 (b, c), the Kramers-Kronig relations appear to work relatively well along the k_m path in the low coupling case. Nevertheless we find that, in this model, failures occur at qualitatively similar couplings when momentum-dependence is added.

CONCLUSIONS

The spectral function is an extremely rich data source. We have shown that, despite its allure, away from the Migdal limit it is not always possible to extract the true microscopic coupling through quasiparticle renormalizations of ARPES data with an effective coupling scheme - and certainly not for cases close to a dispersion maximum. In this limit $\lambda_{\text{eff}} \neq \lambda$. However, through careful modeling and the analysis of specific features it may be possible to learn much more. If one can correctly guess the model it may be possible to predict a given renormalization, or even show experimental support for

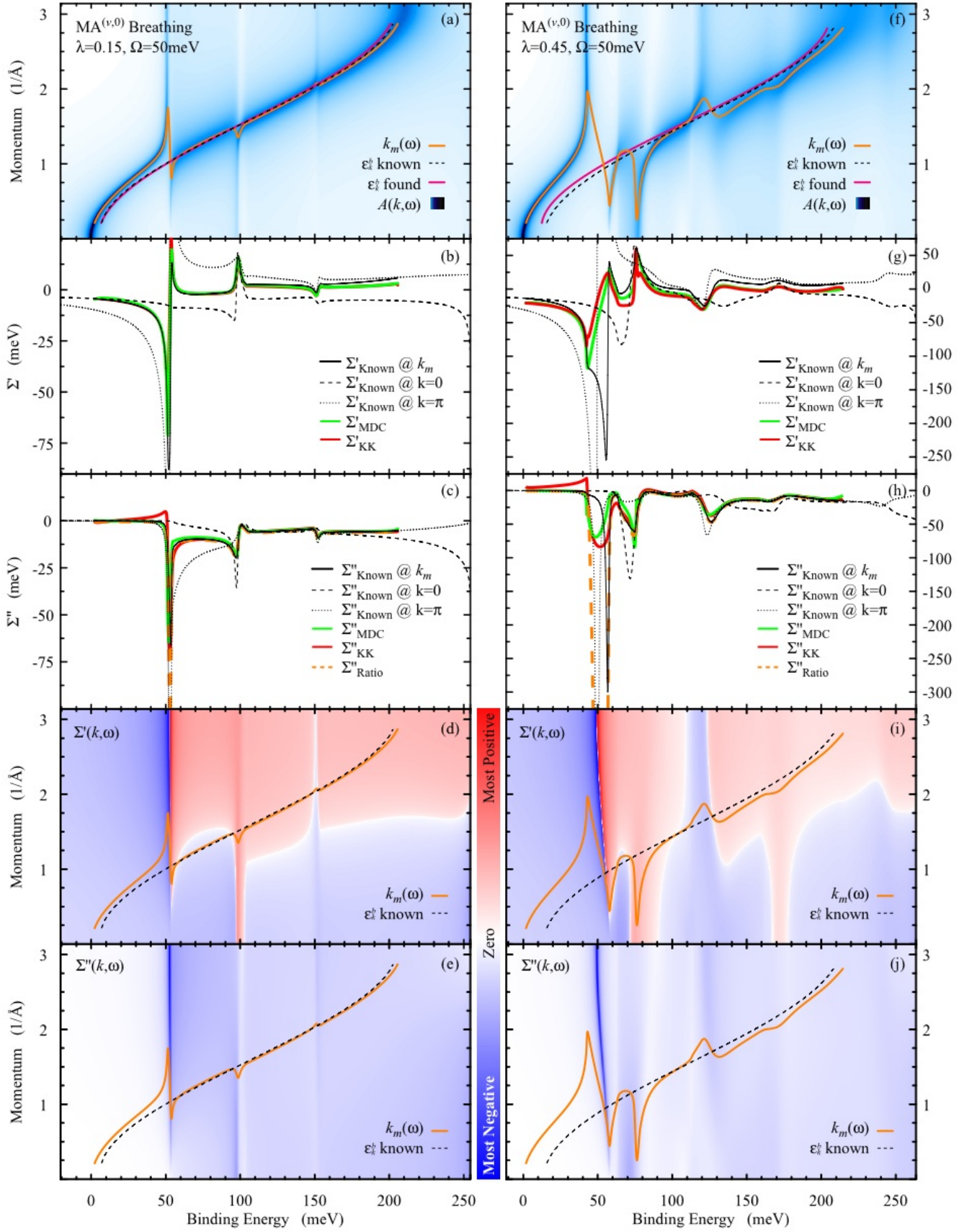


FIG. 10: (Color online). (a-c,f-h) $A(k, \omega)$ and self-energies as defined in Fig. 8 for momentum dependent coupling to a single breathing mode. In this instance, as the self-energy is momentum-dependent, the known self-energies are plotted along the path of peak maxima ($\Sigma'_{\text{Known}} @ k_m$) to show good agreement with the derived values, as well as along both edges of the Brillouin Zone for comparison ($\Sigma'_{\text{Known}} @ k = 0$ and $\Sigma'_{\text{Known}} @ k = \pi$). Finally (d,e,i,j) show the full extent of the energy and momentum-dependence of the real and imaginary self-energies as a false color plot, with the k_m path superimposed.

a given model via relationships between renormalization parameters. Through MDC self-energy analysis, we have shown that the self-energy can be extracted along paths through (k, ω) space in the low coupling regime - and it is possible still to gain some insight at higher couplings. We have also shown that it is possible to infer the momentum-dependence of the self-energy through comparison of renormalization properties. Methods like these, together with detailed models and powerful simulations, will hold the key to more thorough and quantitative analysis of the rich data supplied through ARPES.

APPENDIX ON KKBF

The method outlined here varies slightly from techniques previously described in the literature, which generally reduce the functional form for ε_k^b substantially in order to facilitate an exact solution for $A(k, \omega)$ as they often deal with data very close to the Fermi energy over a small range [12, 22–24]. In our analysis we have instead expanded everything about k_m , essentially using a new linear approximation for ε_k^b on each MDC slice. Although our method has the disadvantage that it does not work as well near the zone boundary where the band velocity goes to zero (other methods which make a second order approximation can successfully predict and fit the non-Lorentzian shape in this region and may continue to work in this regime), ours has the distinct advantage that it works over a much larger energy range and allows fitting based on an infinite variety of bare-band models (so long as they are differentiable). Most importantly, by its form it also explicitly shows that the self-energies are evaluated along the k_m path in the case where there is global momentum-dependence in the self-energy. One might imagine that for the analysis of a particular experiment one may have reasons to choose one method over another, or perhaps even a hybrid of the two. Here we will describe the idea of a Kramers Kronig bare-band fitting (KKBF) as implemented for our method, its application to other methods is similar.

KKBF is a technique whereby a Lorentzian fit is first performed on every slice of constant energy, $\tilde{\omega}$, according to Eq. 8. The values of k_m and Δk_m from the fits can provide the self-energies for every $(\tilde{\omega}, k_m)$ point, within the limitations above, if the bare-band ε_k^b is known. As an analytic complex function the real and imaginary parts of the self-energy are Kramers-Kronig related:

$$\Sigma'_{KK}{}''(k, \omega) = \pm \frac{1}{\pi} \mathcal{P} \int_{-\infty}^{\infty} \partial \xi \frac{\Sigma''_{MDC}(k, \xi)}{\xi - \omega}. \quad (13)$$

It is possible to ‘fit’ the bare-band parameters by choosing them such that $\Sigma'_{MDC} \equiv \tilde{\omega} - \varepsilon_{k_m}^b$ and $\Sigma''_{MDC} \equiv -v_{k_m}^b \Delta k_m$ are self-consistent with Σ'_{KK} and Σ''_{KK} . Since neither the Kramers-Kronig relationships

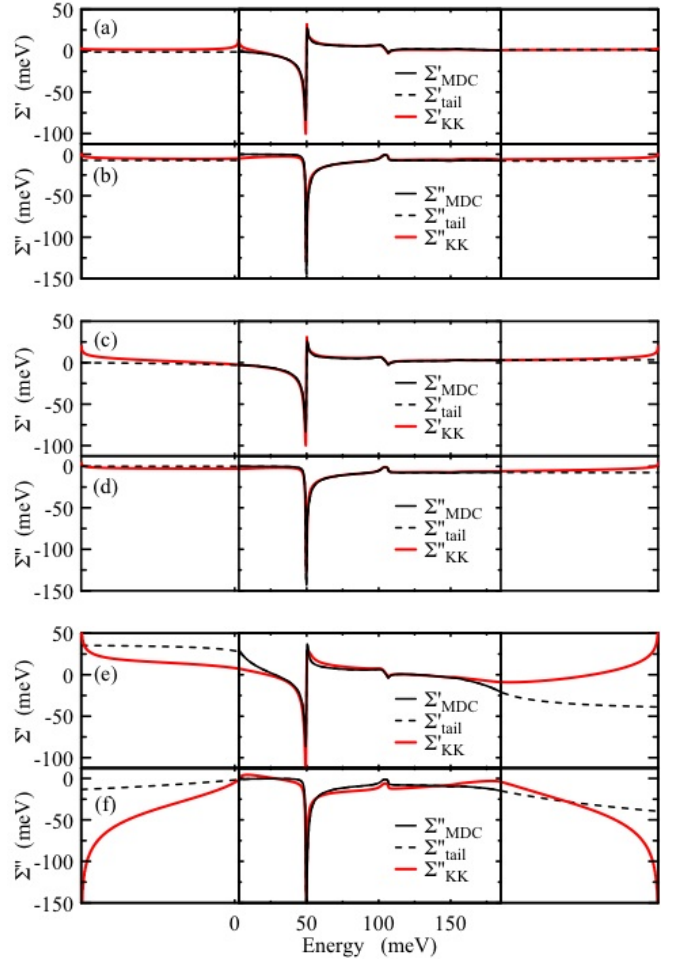


FIG. 11: (Color online). Self-energies as defined in Fig. 8 for the MA⁽¹⁾ Holstein problem with $\Omega = 50$ meV and $\lambda = 0.15$, with extrapolated tails for Σ_{MDC} and the KK transform shown. Panels (a) and (b) have the bias used in fitting the tails set too small, (e) and (f) have the bias set too large, and (c) and (d) have it set just right.

(Eq. 13) nor the MDC relationships (Eq. 10) are sensitive to a constant offset in both the real self-energy and bare-band this is unconstrained by the method and both Σ' and ε_k^b are free. In our study we have simply made the calculation of differences between Σ_{KK} and Σ_{MDC} insensitive to a constant offset, and set the final offset to zero by hand at the end to allow comparison.

In our implementation of this idea, a simple third order polynomial was used to fit the bare-band with an initial guess found by fitting MDC peak maxima. We then used the Levenberg-Marquardt Algorithm [46] as implemented in the mpfit package for IDL [47] to vary band parameters. We found that the standard sum-of-squares minimization on the differences between Σ_{KK} and Σ_{MDC} did not perform as well as a concave-down function, as it placed too much weight on outlying points far away. In order to evaluate the integrals in Eq. 13 with a finite region of data tails were extrapolated before a Fourier-

based transform was performed (the tails were then discarded, leaving the analysis of MDC and KK curves only within the data region). These tails were extrapolated by fitting an inverse polynomials to each side of the data, weighing the fit for each side's tail with an exponentially decaying bias parameter. A bias parameter of zero would weigh the entire curve equally, while a large bias parameter would concentrate only near that data edge.

It is possible for problems such as tails, overweighted outliers, and unconstrained offsets to compound each other. An unconstrained constant offset in Σ'_{MDC} and ε_k^b leads toward a tendency for a small linear offset in both, which when Kramers-Kronig transformed will distort Σ''_{KK} most visibly near the edges of the data, where it can interfere with a good fit of the tails. This in turn can lead to inaccuracies at these edges, which if overweighted can distort the bare-band fit itself. This runaway condition results in a fit which gets progressively worse through iterations and will never find the correct bare-band. In practise we found that the tail bias parameter as well as the the concavity of the function used to process errors must be carefully adjusted by hand in order to prevent this, which can be accomplished simply by looking at whether or not the tail approximation continues to appear reasonable through successive iterations.

In Fig. 11 we show some typical examples of how the tail bias parameter can affect the fitting, each pair of panels represents the final "solution" of the entire band minimization problem using a given tail bias. Plots like these form the guide to be used when adjusting the bias parameters by hand while looking for the best solution. In panels (a) and (b) the tail bias is too small, and so the found tail is the best approximation which fits the whole curve. In panel (b) this causes a discontinuity for the low-energy tail right at the boundary, which in turn causes a cusp in the KK transform visible in (a). Despite this, the overall fit is not too bad with reasonable general agreement between MDC and KK self-energies - meaning the found bare-band is likely close to the real solution. In panels (c) and (d) the tail bias is good, which results with a realistic fit at all boundaries and a good agreement between MDC and KK self-energies giving confidence that the found bare-band is accurate. In panels (e) and (f) the tail bias is too strong, which results in a tail fit depending too much on the data right at the edges. This results in a KK transform which is poor enough to thrown off the band fitting entirely resulting in a found bare-band which is likely not close to the true band, shown by generally poor agreement between MDC and KK self-energies.

ACKNOWLEDGEMENTS

We gratefully acknowledge S. Johnston, T.P. Devereaux, F. Marsiglio I.S. Elfimov, B. Lau, and G.A. Sawatzky for many useful discussions. This work was

supported by the Killam Program (A.D.), Alfred P. Sloan Foundation (A.D.), CRC Program (A.D.), Steacie NSERC Fellowship Program (A.D.), NSERC, CFI, CIFAR Quantum Materials and Nanoelectronics Programs, and BCSI.

* Electronic address: damascelli@physics.ubc.ca

- [1] A. Damascelli, *Physica Scripta* **T109**, 61 (2004).
- [2] T. Valla, A. V. Fedorov, P. D. Johnson, and S. L. Hulbert, *Phys. Rev. Lett.* **83**, 2085 (1999).
- [3] Z.-X. Shen, A. Lanzara, S. Ishihara, and N. Nagaosa, *Phil. Mag. B* **82**, 1349 (2002).
- [4] N. J. C. Ingle, K. M. Shen, F. Baumberger, W. Meevasana, D. H. Lu, Z.-X. Shen, A. Damascelli, S. Nakatsuji, Z. Q. Mao, Y. Maeno, et al., *Phys. Rev. B* **72**, 205114 (2005).
- [5] M. L. Kubic, *Phys. Reports* **338**, 1 (2000).
- [6] G. Mahan, *Many-Particle Physics* (Plenum, 1981), 2nd ed.
- [7] G. Grimvall, *The Electron-Phonon Interaction in Metals* (Elsevier, 1981).
- [8] A. Lanzara, P. V. Bogdanov, X. J. Zhou, S. A. Kellar, D. L. Feng, E. D. Lu, T. Yoshida, H. Eisaki, A. Fujimori, K. Kishio, et al., *Nature* **412**, 510 (2001).
- [9] A. Kaminski, M. Randeria, J. C. Campuzano, M. R. Norman, H. Fretwell, J. Mesot, T. Sato, T. Takahashi, and K. Kadowaki, *Phys. Rev. Lett.* **86**, 1070 (2001).
- [10] T. K. Kim, A. A. Kordyuk, S. V. Borisenko, A. Koitzsch, M. Knupfer, H. Berger, and J. Fink, *Phys. Rev. Lett.* **91**, 167002 (2003).
- [11] N. Mannella, W. L. Yang, X. J. Zhou, H. Zheng, J. F. Mitchell, J. Zaanen, T. P. Devereaux, N. Nagaosa, Z. Hussain, and Z.-X. Shen, *Nature* **438**, 474 (2005).
- [12] A. A. Kordyuk, S. V. Borisenko, A. Koitzsch, J. Fink, M. Knupfer, and H. Berger, *Phys. Rev. B* **71**, 214513 (2005).
- [13] F. Giustino, M. L. Cohen, and S. G. Louie, *Nature* **452**, 975 (2008).
- [14] D. Reznik, G. Sangiovanni, O. Gunnarsson, and T. P. Devereaux, *Nature* **455**, E6 (2008).
- [15] R. Heid, K.-P. Bohnen, R. Zeyher, and D. Manske, *Phys. Rev. Lett.* **100**, 137001 (2008).
- [16] S. Johnston, F. Vernay, B. Moritz, Z.-X. Shen, N. Nagaosa, J. Zaanen, and T. P. Devereaux, *Phys. Rev. B* **82**, 064513 (2010).
- [17] P. Monthoux, *Phys. Rev. B* **68**, 064408 (2003).
- [18] R. J. Wojciechowski, *Physica B*. **259-261**, 498 (1999).
- [19] C. Grimaldi, L. Pietronero, and S. Strässler, *Phys. Rev. Lett.* **75**, 1158 (1995).
- [20] C. N. Veenstra, G. L. Goodvin, M. Berciu, and A. Damascelli, *Phys. Rev. B* **82**, 012504 (2010).
- [21] T. Valla, A. V. Fedorov, P. D. Johnson, B. O. Wells, S. L. Hulbert, Q. Li, G. D. Gu, and N. Koshizuka, *Science* **285**, 2110 (1999).
- [22] A. Damascelli, Z. Hussain, and Z.-X. Shen, *Rev. Mod. Phys.* **75**, 473 (2003).
- [23] J. C. Campuzano, M. R. Norman, and M. Randeria, *Photoemission in the High T_c Superconductors* (Springer, Berlin, 2004), vol. II, pp. 167-265.
- [24] A. Kaminski and H. M. Fretwell, *New J. Phys.* **7**, 98

- (2005).
- [25] E. G. Maksimov, M. L. Kubic, and O. V. Dolgov, *Adv. Cond. Mat. Phys.* (2010), article ID 423725.
- [26] M. Randeria, A. Paramakanti, and N. Trivedi, *Phys. Rev. B* **69**, 144509 (2004).
- [27] A. Migdal, *Sov. Phys. JETP* **34**, 996 (1958).
- [28] P. Werner and A. Millis, *Phys. Rev. Lett.* **99**, 146404 (2007).
- [29] A. Knigavko and J. P. Carbotte, *Phys. Rev. B* **72**, 035125 (2005).
- [30] E. Cappelluti and L. Pietronero, *Phys. Rev. B* **68**, 224511 (2003).
- [31] M. Berciu, *Phys. Rev. Lett.* **97**, 036402 (2006).
- [32] M. Berciu and G. L. Goodvin, *Phys. Rev. B* **76**, 165109 (2007).
- [33] G. L. Goodvin and M. Berciu, *Phys. Rev. B* **78**, 235120 (2008).
- [34] T. Holstein, *Ann. Phys.* **8**, 325 (1959); *ibid.*, **8**, 343 (1959).
- [35] M. Eschrig and M. R. Norman, *Phys. Rev. B* **67**, 144503 (2003).
- [36] B. Lau, M. Berciu, and G. A. Sawatzky, *Phys. Rev. B* **76**, 174305 (2007).
- [37] Z. Li, D. Baillie, C. Blois, and F. Marsiglio, *Phys. Rev. B* **81**, 115114 (2010).
- [38] A. Alvermann, H. Fehske, and S. A. Trugman, *Phys. Rev. B* **81**, 165113 (2010).
- [39] M. Capone, S. Ciuchi, and C. Grimaldi, *Europhys. Lett.* **42**, 523 (1998).
- [40] M. Capone, W. Stephan, and M. Grilli, *Phys. Rev. B* **56**, 4484 (1997).
- [41] F. Marsiglio, *Physica C* **244**, 21 (1995).
- [42] G. Lepage, *J. Comput. Phys.* **27**, 192 (1978).
- [43] G. Lepage, Cornell preprint CLNS **80**, 447 (1980).
- [44] M. Galassi, J. Davies, J. Theiler, B. Gough, G. Jungman, P. Alken, M. Booth, and F. Rossi, *GNU Scientific Library Reference Manual - Third Edition (v1.15)* (Network Theory Ltd, 2011).
- [45] C. Kim, W. Kyung, S. Park, C. Leem, D. Song, Y. Kim, S. Choi, W. Jung, Y. Koh, H. Choi, et al., *Journal of Physics and Chemistry of Solids* **72**, 556 (2011).
- [46] J. J. More, *The Levenberg-Marquardt algorithm implementation and theory*, vol. 630 of *Lecture Notes in Mathematics* (Springer, 1978).
- [47] C. B. Markwardt, arXiv:0902.2850 (2009).
- [48] With more terms kept exactly, $MA^{(v,1)}$ should show overall improvement over $MA^{(v,0)}$, however for reasons which are not understood it only does so in the quasiparticle regime - conversely the continuum of $A(k, \omega)$ below the quasiparticle band is worsened; toward the Brillouin zone edge it is pushed further down in energy than exact diagonalization results indicate it should be [33, 36]. As the MDC based self-energy analysis uses $A(k, \omega)$ in both the continuum and quasiparticle regime for it we use the lower order $MA^{(v,0)}$.
- [49] In most implementations, the coupling is found via a scattering integral around the Fermi surface [6], which for the breathing-mode model would be zero at all coupling strengths. We take the Brillouin zone as a sensible alternative in this case (the choice is irrelevant for the momentum-independent Holstein coupling).